6

Functional alkoxysilane mediated synthesis of multimetallic analogues of PdNPs

---

6.1. INTRODUCTION

Designing the Pd-based nanodimensional catalysts is of appreciable importance because of their remarkable catalytic properties (Quiros et al., 2002; Chen et al., 2011). The rational tailoring of structural features and composition of nanoscaled Pd-based materials might further enhance the catalytic performance. Current investigations in the area of nanoparticle synthesis indicate that bimetallic and trimetallic nanoparticles are catalytically more proficient over monometallic counterparts (Liu et al., 2014; Gan et al., 2012). Multilayered core-shell nanoparticles with precisely restrained morphological characteristics have become increasingly significant, and contribute favourable possibilities to satisfactorily refine the catalytic response of metal nanoparticles (Mun et al., 2013; Kang et al., 2013). The nanostructured systems having Au, Pd, Pt and Ag as the constituent metals (Cha et al., 2015), are particularly interesting due to their superior properties (Yang et al., 2018). For example, combinations like Au@Pd, Au@Pt, Pt@Pd, and Pd@Pt core-shell bimetallic colloids (Sun et al., 2017) have been explored widely for exclusive crystallographic, electronic, optical and catalytic properties, which are not achievable in monometallic form. Lim et al (2009) claimed that bimetallic counterparts of Pt like Pd@Pt,

Au@Pt, exhibit raised tolerance for carbon monoxide in formic acid fuel cell, and high turnover frequency for oxygen reduction reaction (ORR) (Brodsky et al., 2014). Regardless of advancements in the synthetic routes employed for designing the multicompositional core shell nanostructures (Choi et al., 2012), it has been documented that most of the reported methods involve complex multistep growth mechanism which often result in nanoclusters with certainly unregulated nucleation and aging. Accordingly, there is a need to formulate a simple one pot synthetic route (Kang et al., 2013), to obtain multiple layered core-shell nanoparticles with diverse compositions.

This chapter describes a facile way to synthesize Ag@Ru@Pd, triple layered nanostructure where Pd constitutes the innermost spot, while Ru and Ag form the subsequent layers, under the bifold action of organofunctionalised alkoxysilanes (EETMS) and polymeric stabilizer (PVP) using template approach. The fabrication advances through sequential pathway, following the seed mediated growth phenomenon, where presynthesized PdNPs act as seed to produce Ru@PdNPs, which are in turn the ready-seeds to obtain the desired trimetallic nanocrystals of Ag@Ru@PdNPs. As discussed in previous chapters, the alkoxysilanes and PVP synergistically behave as precise structural directing agents to prepare homogenous and well stabilized nanoparticles with multiple compositions. Alkoxysilanes like 3-aminopropyltrimethoxysilane (APTMS), (Bartholome et al., 2005) 3-glycidoxypropyltriethoxysilane (GPTMS), 2-(3,4-epoxycyclohexyl) ethyltrimethoxysilane (EETMS) and trimethoxysilane (TMS) are widely known for generating nanostructured matrix of ormosils through holding control over the hydrophobicity and hydrophilicity of organosilanes (Pandey et al., 2003, Pandey et al., 2001). The role of APTMS in the controlled synthesis of functional noble metal nanoparticles like

AuNPs, AgNPs and PdNPs has been thoroughly explored in our previous reports (Pandey and Pandey, 2014; Pandey and Singh, 2015; Pandey and Pandey, 2016). Similarly, the role of another alkoxysilanes, likewise GPTMS, (Lakshminarayana and and M. Nogami, 2009) in developing Pd linked glycidoxy moiety has been widely accepted, for evolving Pd-linked ormosil having aptitude in biocatalysis (Tripathi et al., 2006). (Pandey et al., 2014). (Pandey et al., 2004). Similarly, the stabilizing and reducing ability of EETMS (Jabbour et al., 2008; Briche et al., 2008) has been examined efficiently in the previous chapters, for synthesizing mono and bimetallic analogues of palladium nanoparticles.

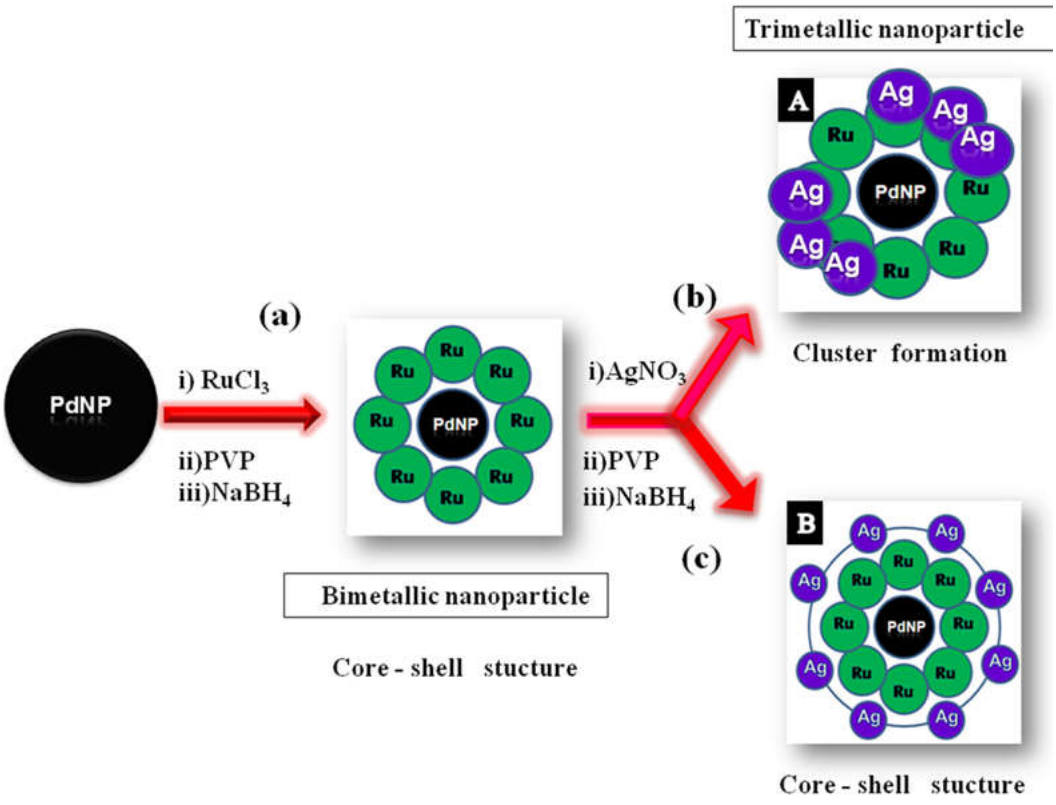

Scheme 6.1. Schematic illustration of seed mediated nucleation of heterometallic nanocrystallites by two step reduction approach. (a) Formation of bimetallic core–shell nanocrystal (Pd@Ru) while (b and c). Growth of corresponding trimetallic nanoparticles.

In this chapter we expand our concept to further describe that trimetallic Au@Ru@Pd nanoparticles can be synthesized by using PVP and EETMS as typical stabilizing and structure directing agents.The previous findings on the encapsulation of active materials into the nanostructured framework of sol-gel (ormosil) thin film, and its effective utilization as the heterogeneous catalyst for several electrochemical sensing applications, directed the conversion of as-synthesised nanoparticle colloids into catalytically active thin films. The presence of alkoxysilane (EETMS) led to the compatible interaction of PdNPs, Ru@PdNPs and Ag@Ru@PdNPs with ormosil solution. Accordingly, it was intended to prepare the nanoparticle linked sol-gel thin films via sonication, and based on the presence of different nanoparticles, four types of modified electrode systems (I-IV) are suitably designed by encapsulating the potassium ferricyanide $[Fe(CN)_6]^{3-/4-}$. Prepared electrode systems are observed to be promising materials for heterogeneous catalysis. The electrocatalytic oxidation of ascorbic acid (AA) has been investigated using nanoparticle modified electrodes, as discussed in the chapter.

6.2. EXPERIMENTAL DETAILS

6.2.1. Materials

Potassium tetrachloropalladate(II) (K_2PdCl_4, 2-(3,4-epoxycyclohexyl)ethyltrimethoxysilane, ruthenium trichloride(III) hydrate ($RuCl_3 \cdot xH_2O$), silver nitrate ($AgNO_3$), sodium tetrahydroborate ($NaBH_4$), and polyvinylpyrrolidone (PVP), HCl, potassium ferricyanide and L-Ascorbic acid were obtained from Sigma Aldrich.

6.2.2. Synthesis of Ag@Ru@PdNPs

Palladium nanoparticles are synthesized as discussed so far in former chapters. Typical synthesis involves: the solutions of PVP (10 μL, 1 %) and K_2PdCl_4 (50 μL, 10 mM) were mixed followed by the addition of EETMS (10 μL, 2.5 M), mixture was stirred over vertex cyclomixer, and incubated at about 45 ºC, for 10-15 min. Brownish-black colloidal solution of palladium nanoparticles was obtained. Further, the methanolic solution of $RuCl_3$ (50 μL, 10 mM) was added to the above synthesized palladium nanoparticle dispersion (50 μL), after gentle mixing PVP (10 μL) was added, further $NaBH_4$ (2 μL, 0.01 M) was added dropwise, after stirring for few minutes, a clear dark brownish-black dispersion of bimetallic nanoparticles was produced at room temperature.

Further the trimetallic nanoparticles were synthesized as: the solutions of silver nitrate (30 μL, 10 mM) and PVP (10 μL) were added to as synthesized bimetallic colloidal solution of Ru@Pd (∼100 μL), followed by the careful addition of $NaBH_4$ (2 μL, 0.01 M), and on vigorous stirring, transparent yellowish-black colloidal solution of Ag@Ru@Pd was obtained.

6.2.3. Characterization of trimetallic nanoparticles

UV-VIS investigations were carried out using HITACHI U-2900 spectrophotometer. Measurements were done in 1 cm quartz cuvette in the wavelength range of 200–800 nm. TEM results were obtained by Hitachi 80, with an accelerating voltage of 200 kV. AFM studies were brought about by NT-MDT, NTEGRA TRIMA with scanning mode—semi contact/tapping mode, with monochromatic laser beam of wavelength 650 nm and frequency 150 Hz. EDS

profile was obtained from ZEISS oxford Instrument S1- ADD0048 (USA). XPS results were obtained by KRATOS, Amicus instrument using Al anodes producing Kα–X-rays.

6.2.4. Electrochemical investigations

Electrochemical measurements were performed on CHI830b Electrochemical Analyser using three electrode systems with a working volume of 3 mL, containing thin film coated glassy carbon electrode as the working electrode, platinum plate auxiliary electrode and an Ag/AgCl as reference electrode. Cleaned glassy carbon electrodes were coated with nanoparticle encapsulated thin film, with composition: APTMS (5.41 M), 2-(3, 4-epoxycyclohexyl) ethyltrimethoxysilane (4.32 M) and HCl (0.1 M) and other additives as reported in Table 6.1.

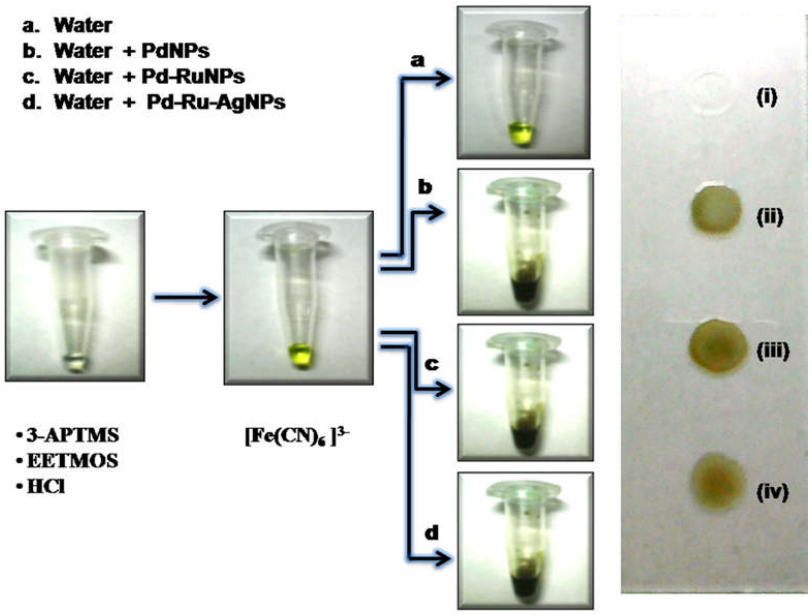

Scheme 6.2. Flow scheme showing fabrication of electrodes, following step wise addition of different additives in optimised ratios.

Precursors were mixed in desired ratios and solutions obtained were sonicated for atleast 10 minutes to homogenize the contents, films were finally dried at room temperature.

6.3. RESULTS

6.3.1. Synthesis of multilayered nanoparticles

Palladium nanoparticles were fabricated as discussed in previous chapters, by following the modified synthetic route which involved EETMS as an efficient reducing and capping agent. EETMS functionalized PdNPs are effectively used as seeds for preparing bimetallic nanoparticles, in combination with other alkoxysilanes like APTMS, as illustrated in last chapter (V). Also the role APTMS in synthesising an array of mono and multimetallic nanoparticles in the presence of various organic reducing agents has been well documented in our previous reports (Pandey and Singh; 2014; Pandey and Pandey, 2016). Taking into account, the results of these findings, it was intended to explore the role of functionalized PdNPs in preparing the multilayered nanoscaled structures, using seeded growth strategy. Here, successive metal (Ru, Ag) nanoparticles are allowed to grow on pre-synthesized discrete palladium nanoparticles. Scheme 6.1 visualises the synthetic pathway followed to produce multimetallic nanoparticles. In this two step synthetic route, the sequential addition and reduction of respective metal salt at each stage led to the formation of successive layers. The product thus obtained was monodispersed as individual nanoparticles are homogenously distributed throughout. Opaque shell like arrangement of Ru in BNPs and Ag in TNPs, happen to cover the bigger particles of PdNPs and binary Ru@Pd atoms, during the corresponding synthesis. The bimetallic nanoparticles are assembled into explicit core–shell architecture, while the trimetallic

nanoparticles adopted heterogeneous assembling either into core–shell or other random cluster like orientations, as evident from the TEM images (Figure 6.2-6.4).

6.3.2. Characterisation of triple-layered nanoparticles

UV-Vis spectroscopy gives the preliminary insight into the synthesis of nanoparticles by the appearance or disappearance of dishtinguishing peaks. The formation of PdNPs is marked by the disappearance of the characteristic peaks of Pd^{2+}, generally observed at 320 nm and 425 nm while a trail with increasing absorbance is recorded (Figure 6.1). Similarly, for Ru@Pd(BNPs), the well defined peak of Ru^{3+} at 380 nm disappeared, when Ru^{3+} was completely reduced to Ru^{0}. For Ag@Ru@Pd(TNPs) the absorbance maxima lie at ~420 nm which corresponds to the characteristic band of silver nanoparticles.

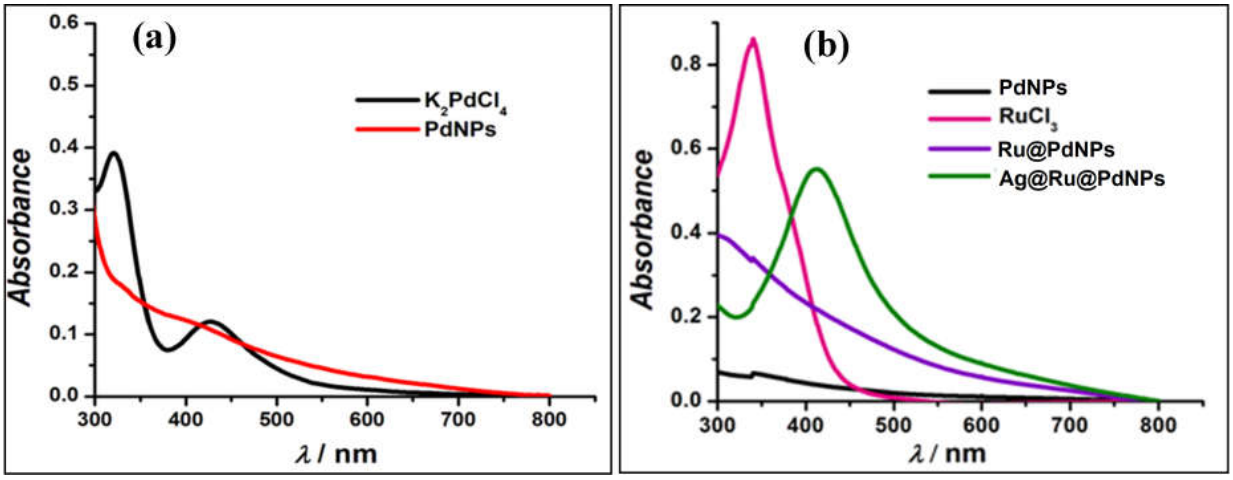

Figure 6.1. UV spectrum of (1) Pd nanoparticles (2) bimetallic and trimetallic nanocomposites.

TEM image of PdNPs (Figure 6.2a) shows the uniformly spread particles having irregular shapes, with an average diameter of 8.8 nm. TEM images of BNPs and TNPs are shown in Figures 6.3-6.4, further indicate that Ru@PdNPs exhibit core–shell framework while

Ag@Ru@PdNPs possess mixed features of core-shell structure as well as of cluster like configuration. BNPs exhibit an average diameter of 3.4 nm and are homogenously distributed with a nominal sign of aggregation. While the random structures of TNPs possess an average particle size of 6.8 nm. SAED pattern of PdNPs shows a dotted ring arrangement (Figure 6.2b) which confirms the polycrystalline nature of the palladium nanoparticles. The four visible rings in diffraction pattern are assigned with lattice planes as (220), (311), (422), (531) which clearly denote the FCC lattice of PdNPs.

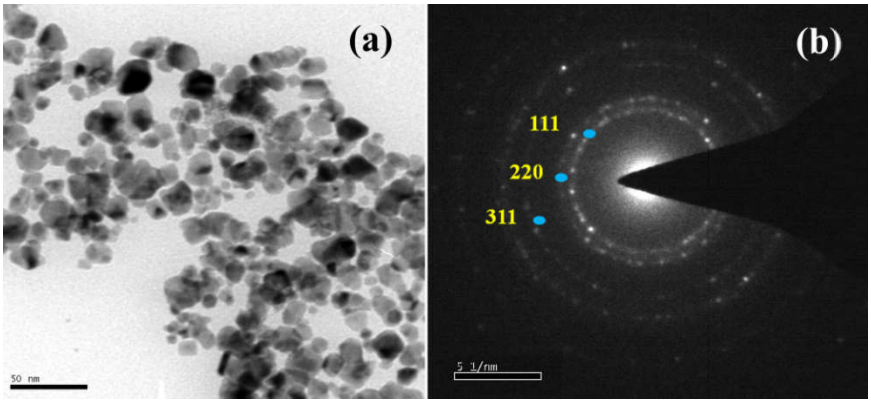

Figure 6.2. TEM image (a), SAED pattern (b) of PdNPs.

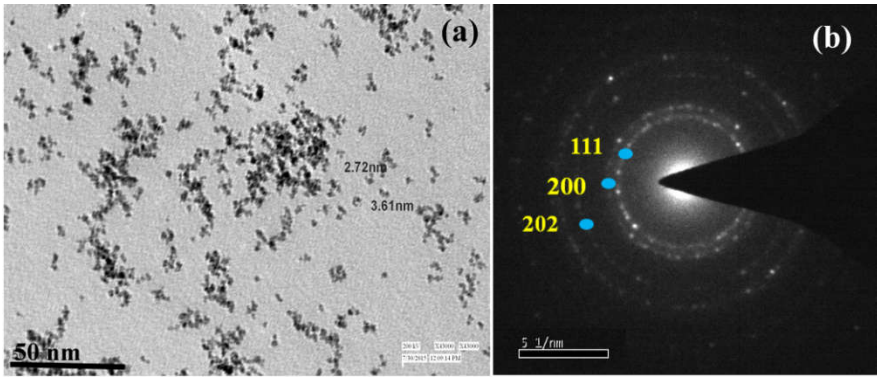

Figure 6.3. TEM image (a), electron diffraction pattern of (b) Ru@PdNPs.

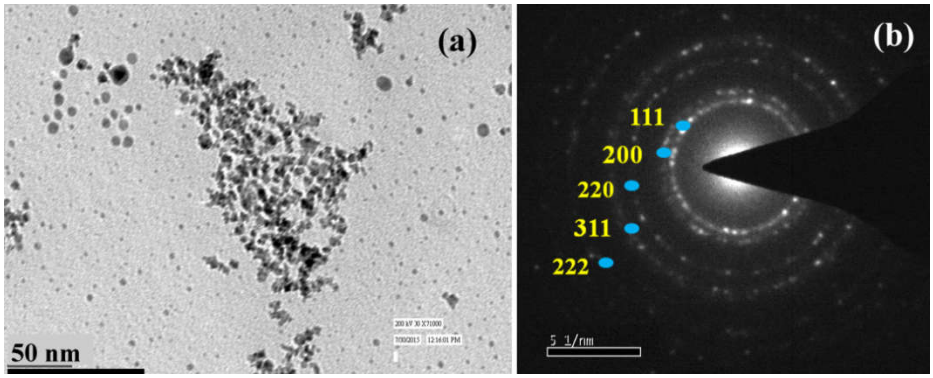

Figure 6.4. TEM image (a), electron diffraction pattern of (b) Ag@Ru@PdNPs.

Diffraction pattern of bimetallic Ru@PdNPs presents a sharp orientation of Bragg spots or Debye rings, and the corresponding lattice planes assigned are (111), (200) and (202). Similarly, the lattice planes in case of Ag@Ru@PdNPs are, (111), (200), (220), (311) and (222).

EDS spectrum displayed in Figure 6.5a, shows two peaks (major one at 2.8 eV while a weak peak at ~3.6 eV) corresponding to Pd metal. Similarly, the EDS profile shown in Figure 6.5b, belongs to BNPs, with specific peaks of Pd and Ru, at 3.2, 3.4, 2.2 (major peak of Ru) and 2.8 eV, proved the existence of Pd and Ru, analogously, Figure 6.5c affiliates to TNPs, as it favourably remarks the presence of Pd, Ru and Ag with a sharp unique peak at 2.6 eV, and other subsidiary peaks at 3 eV (Ag), 2.2 and 3.2 eV (Ru), and 3.6 eV (Pd) respectively. Thus, it was proved that the Ag@Ru@Pd triple layered nanoparticles were successfully synthesized by the one-step facile synthetic route in EETMS and PVP based solution at room temperature. Elemental mapping profile of nanoparticles shown in Figures 6.6-6.7 further confirm the formation of three layers corresponding to Ru in Ru@PdNPs and Ru, Ag in Ag@Ru@PdNPs.

The fabricated nanoparticles are probed with XPS using synchrotron radiation (Zheng and Stucky; 2006).

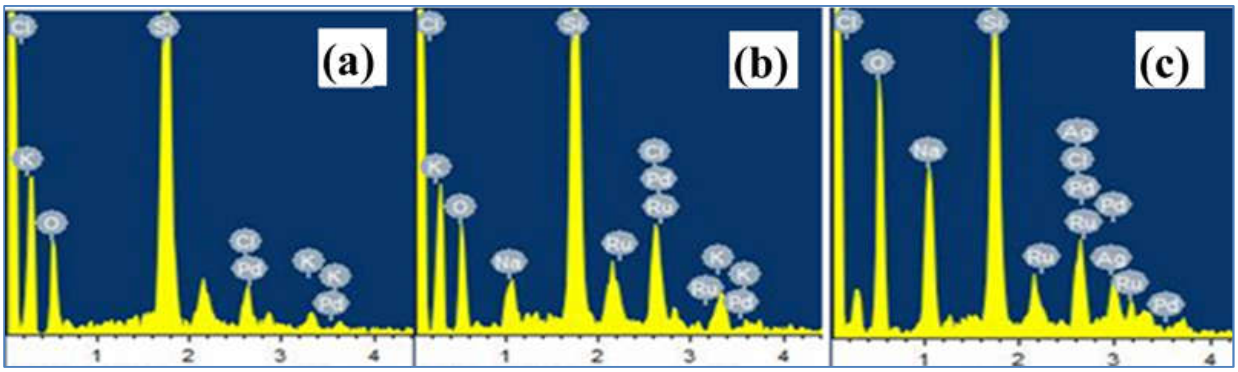

Figure 6.5. EDS spectra of PdNPs (a), Ru@PdNPs (b) and Ag@Ru@Pd (c) respectively at corresponding binding energies.

The fitted curves in Figure 6.8 show the XPS spectra of palladium in PdNPs, Ru@PdNPs and Ag@Ru@PdNPs. A doublet is obtained for Pd in PdNPs, with peaks $3d_{5/2}$ and $3d_{3/2}$ at binding energies 335 and 340 eV and the standard intensity ratio of 2:3 ($3d_{3/2}$:$3d_{5/2}$) is attained (Moulder et al, 1995).

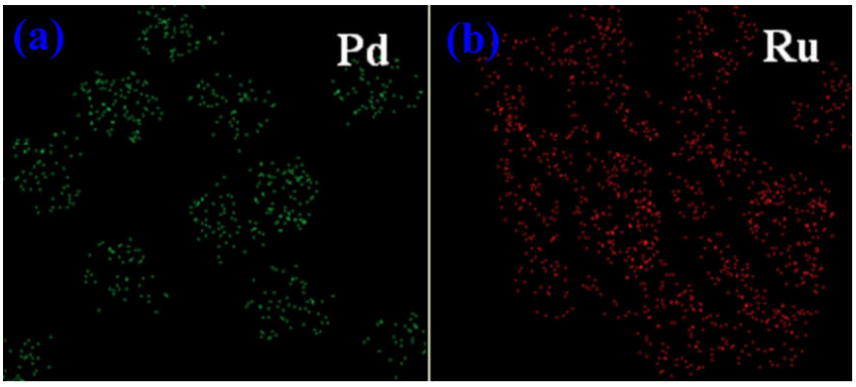

Figure 6.6. Elemental maps of (a) Pd, (b) Ru in bimetallic Ru@Pd nanoparticles.

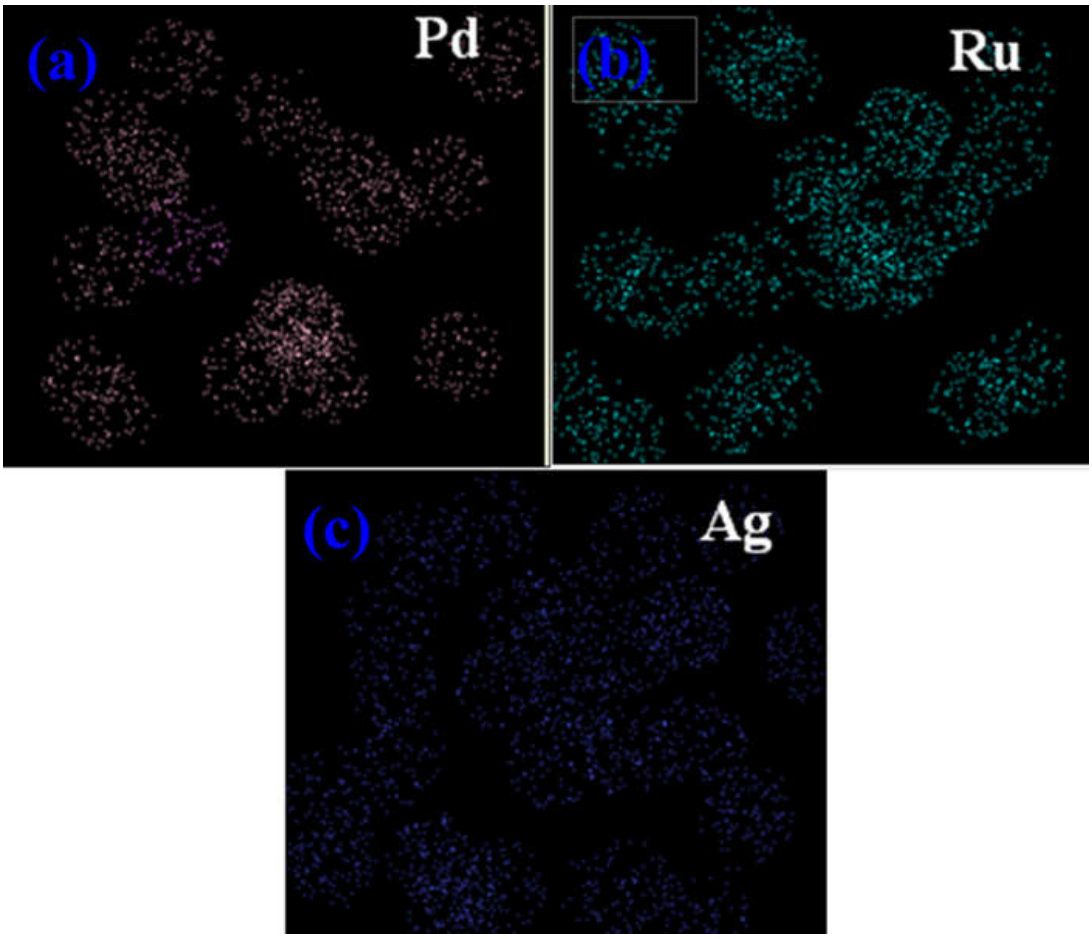

Figure 6.7. Elemental maps of (a) Pd, (b) Ru and (c) Ag in trimetallic Ag@Ru@Pd nanoparticles.

Upon addition of Ru and Ag, the Pd $3d_{5/2}$ peak of Ru@PdNPs is shifted to lower while Pd $3d_{3/2}$ peak of Ag@Ru@PdNPs to higher binding energies. Also the intensity ratios of the peaks deviate from that of the standard value (2:3). Further, spectra of Ru in BNPs (Ru@PdNPs) and TNPs (Figure 6.9a-b), show peak broadening, where the usual peaks [$3d_{5/2}$ (279.8 eV) and $3d_{3/2}$ (284.0 eV)] appear to merge into a single outstretched peak. Similarly, from the spectra of Ag 3d (Figure 6.9c) in case of TNPs, binding energies of the peaks $3d_{5/2}$ and $3d_{3/2}$, are 368.08 eV

and 374.26 eV respectively, which are 0.08 and 0.26 eV higher than the core levels of bulk Ag crystals (368 and 374 eV).

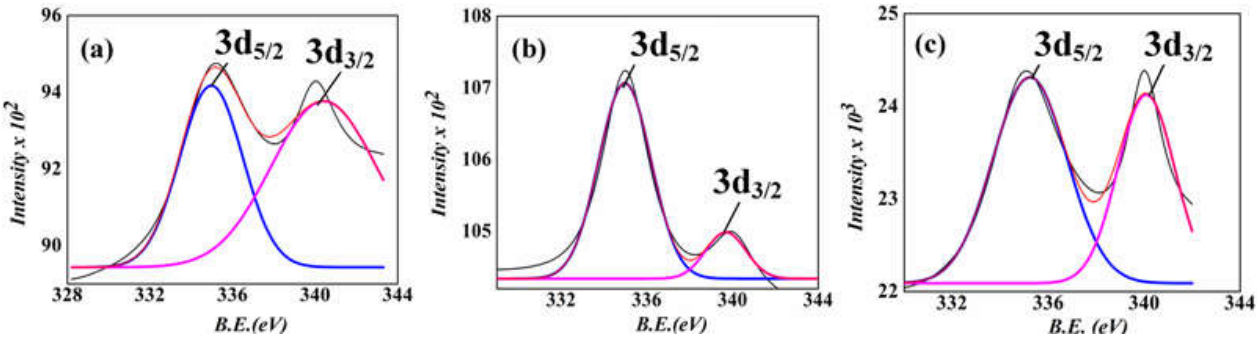

Figure 6.8. XPS spectra of Palladium in monometallic (PdNPs) (a) corresponding bimetallic nanoparticles (Ru@Pd) and in (c) trimetallic nanoparticles (Ag@Ru@Pd).

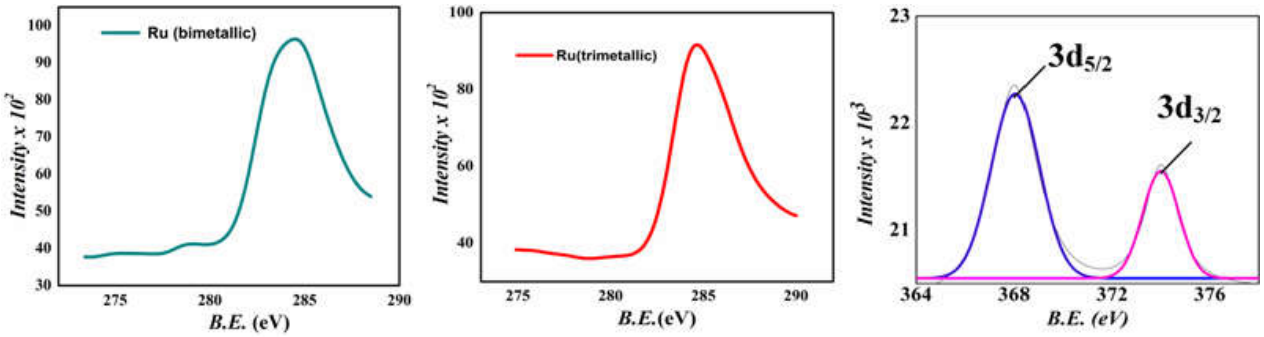

Figure 6.9. XPS spectra of Ruthenium in Ru@PdNPs (a) and Ag@Ru@PdNPs (b). Spectrum of Silver in Ag@Ru@PdNPs (c).

6.3.3. Fabrication of nanomaterial linked organosilicate modified silicates

The thin films of nanoparticle (PdNPs, Ru@PdNPs and Ag@Ru@PdNPs) modified sol-gel glass are casted on glassy carbon electrodes. The as-synthesized nanomaterials are encapsulated into the nanostructured domains of organically modified silicates (ORMOSIL) in order to obtain

electrocatalytically active electrode surfaces. The ormosil thin film is formed by using the homogeneous suspension of 3-aminopropyltrimethoxysilane (APTMS), 2-(3,4-epoxycyclohexyl) ethyltrimethoxysilane (EETMS), HCl along with colloidal solution of nanoparticles as described in Table 6.1. The mixtures were sonicated for 10-15 min, to homogenize the contents. The redox couple like potassium ferricyanide $[Fe(CN)_6]^{3-/4-}$ was added to obtain four different types of electrode systems as summarized in Table 6.1.

Table 6.1. Compositions of four different types of electrode systems

Systems	**I**	**II**	**III**	**IV**
APTMS +EETMS + HCl	20μL + 5 μL +5 μL	20 μL + 5 μL + 5 μL	20 μL + 5 μL + 5 μL	20 μL + 5 μL + 5 μL
$Fe(CN)_6^{3-/4-}$	25 μL	25 μL	25 μL	25 μL
DD water	70 μL	20 μL	20 μL	20 μL
PdNPs	---	50 μL	---	---
Ru@PdNPs	---	---	50 μL	---
Ag@Ru@PdNPs	---	---	---	50 μL

6.3.4. AFM analysis of nanoparticle linked Ormosil Films

Figures 6.10 show the three dimensional view of AFM images of nanoparticle (MNPs/BNPs/TNPs) modified thin films of ormosil on glass substrates (Pandey and Prakash, 2014). It is observed that all the films have uniform surface topography with homogeneous

distribution of nanoparticles, with no sign of cracks and voids. The surface profile parameters of the nanoparticle doped films change according to the composition of the constituents incorporated in different thin films (systems I-IV). The root mean square roughness (R_{sq}) is lowest (0.059 nm) for the film encapsulated with TNPs in comparison to the other systems. The average grain size is found to decrease in the order I<II<III<IV, as outlined in Table 6.2.

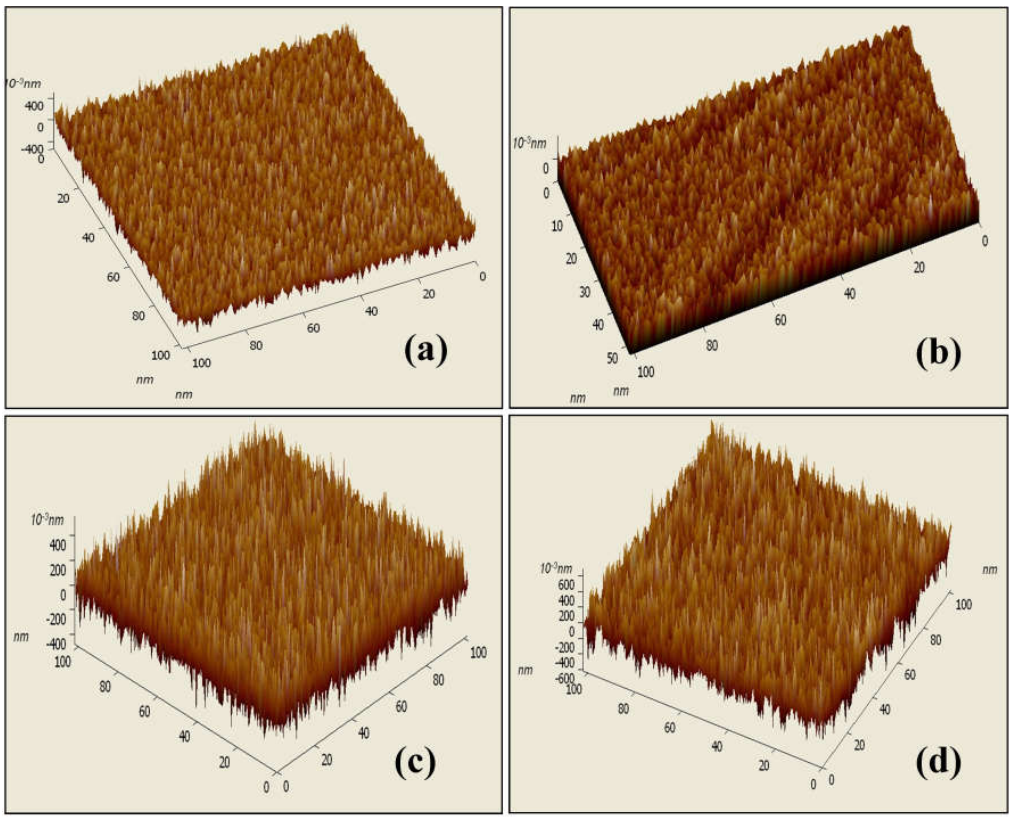

Figure 6.10. AFM images of potassium ferricyanide encapsulated Ormosil (a), Ormosil-PdNPs (b), Ormosil-Ru@PdNPs (c) and Ormosil-Ag@Ru@PdNPs.

6.3.5. Redox electrochemistry of nanoparticle modified electrodes

Further, the investigations on the role of nanoparticle linked ormosil in electrocatalytic applications were recorded (Hu and Dong, 2006). Primarily the redox electrochemistry of

$[Fe(CN)_6]^{3-/4-}$ was studied, when enclosed within the ormosil (Ciriminna et al., 2013). As documented in our previous reports, the nanostructured sol-gel matrices provide enhanced exposure (Dash et al., 2008) to the analyte and increase the electron transfer rate (Pandey et al., 2001; Pandey et al., 2004). Findings on similar lines, directed the attention to investigate the behavior of redox couple in the presence of catalytic materials like nanoparticles inside a sol-gel film. It is observed that incorporation of nanoparticles (PdNPs, Ru@PdNPs and Ag@Ru@PdNPs) particularly Ag@Ru@PdNPs (Figure 6.11d) shows the significant improvement in redox electrochemistry. Figure 6.11 shows the voltammograms of $[Fe(CN)_6]^{3-/4-}$ encapsulated (a) Ormosil, (b) Ormosil-PdNPs, (c) Ormosil-Ru@PdNPs, (d) Ormosil-Ag@Ru@PdNPs, in phosphate buffer at pH.

Table 6.2. Summarized topographical features of different ormosil films obtained through AFM scans.

Systems	**Average grain size (nm)**	**RMS roughness (nm)**	***Height***
I	1.545	0.198	0.750
II	1.538	0.106	0.589
III	1.520	0.083	0.470
IV	1.405	0.059	0.413

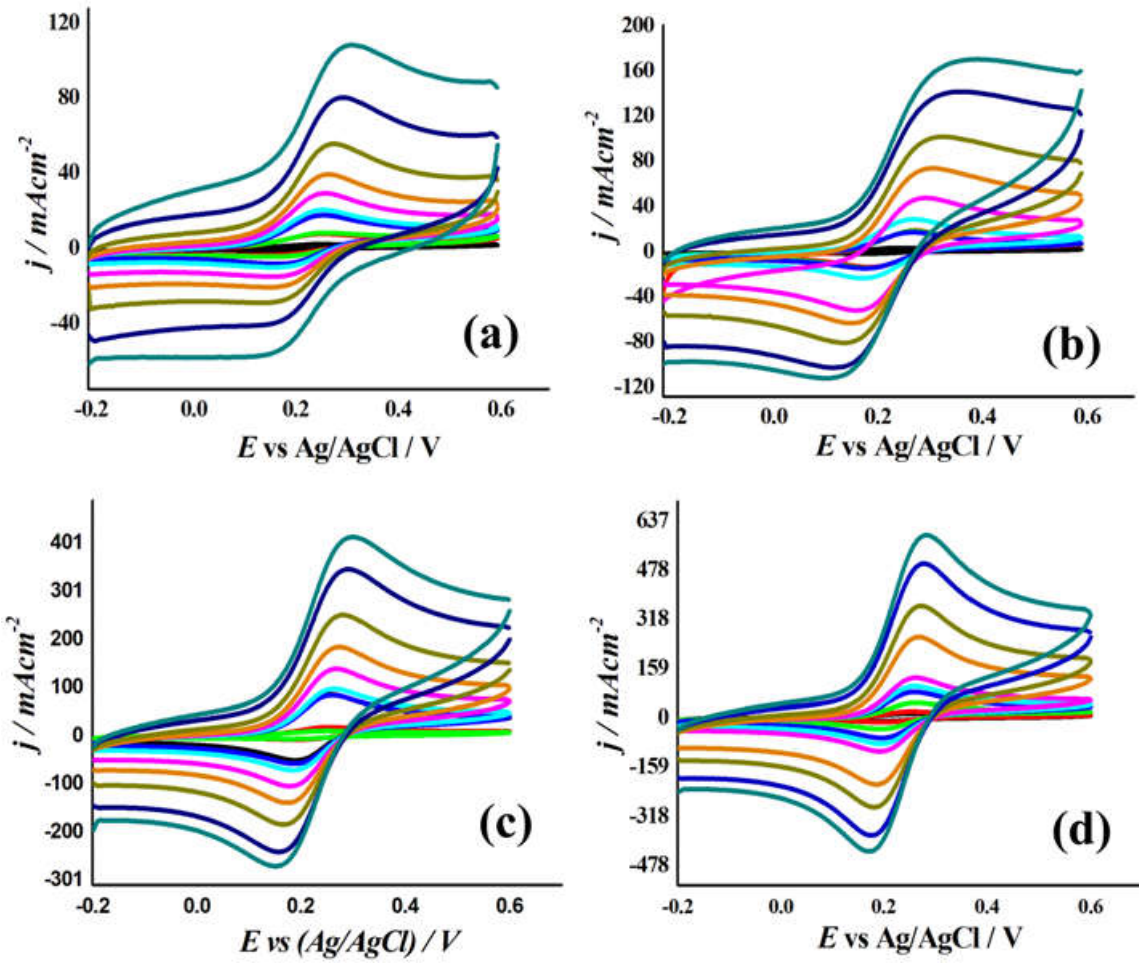

Figure 6.11. Cyclic voltammograms of $Fe(CN)_6^{3-/4-}$ encapsulated within ormosil (a), ormosil-PdNPs (b), ormosil-Ru@PdNPs (c) and ormosil-Ag@Ru@PdNPs modified electrodes in 0.1 M phosphate buffer pH 7 containing 0.5 M KCl at the scan rates between 1-600 mVs^{-1}.

The peak separation has been found to be 180 mV for ormosil, 160 mV for Ormosil-PdNPs, 100 mV for Ormosil-BNPs and 85 mV for Ormosil-TNPs, which clearly justify the improvement in redox electrochemistry over the nanoparticle modified electrodes as a function of the multiplicity of nanoscaled layers of the metals (Pd, Ru and Ag) present.

6.3.6. Electrooxidation of Ascorbic acid

The nanostructured sol-gel thin films enclosed with mono (PdNPs) and multimetallic (Ru@PdNPs and Ag@Ru@PdNPs) noble metal nanoparticles, which are known for their catalytic potential, act as heterogeneous catalyst for the present study. The catalytic performance of these nonoparticle linked ormosil thin film modified electrode systems was evaluated by the heterogenous catalytic oxidation of AA (Bossi et al., 2000; Turkusic et al., 2000) at physiological pH.

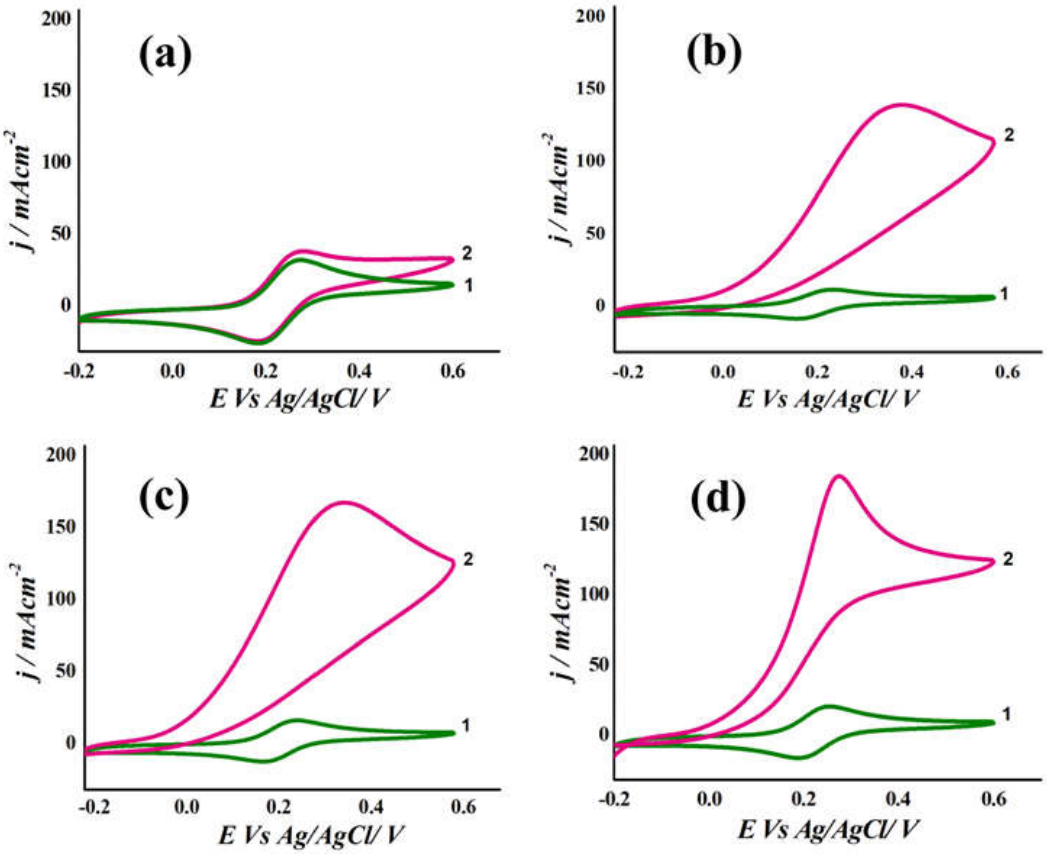

Figure 6.12. Cyclic voltammogram of $Fe(CN)_6^{3-/4-}$ encapsulated (a) Ormosil, (b) Ormosil-PdNPs, (c) Ormosil-Pd-RuNPs and (d) Ormosil-Pd-Ru-AgNPs in absence (1), and presence (2) of Ascorbic acid (1 mM, 30 L) in phosphate buffer (.1 M, pH 7.0) at a scan rate of 10 mV/s.

Figure 6.12 shows the cyclic voltammograms of the oxidation of AA on (a) Ormosil-$[Fe(CN)_6]^{3-/4-}$, (b) Ormosil-$[Fe(CN)_6]^{3-/4-}$-PdNPs, (c) Ormosil-$[Fe(CN)_6]^{3-/4-}$-Ru@PdNPs and (d) Ormosil-$[Fe(CN)_6]^{3-/4-}$-Ag@Ru@PdNPs respectively. The oxidation of AA on all the four electrode systems at a potential of ~0.15 V, increased the anodic current density in the order of I < II < III < IV. The fastest electrocatalytic oxidation of AA was observed to occur on system IV (with TNPs) and at relatively lower potential (Figure 6.12).

6.4. DISCUSSION

6.4.1. Role of alkoxysilanes in synthesis of multimetallics

The EETMS being mild reducing agent, it facilitated the slow and continuous nucleation and thereby resulted in palladium nanoclusters with low surface energy. Initially synthesized PdNPs successfully led to the epitaxial growth of corresponding outer layers on their surface. The synergistic action of EETMS along with polymeric chain stabilizer, tend to control the nucleation, growth and stabilisation of the sequentially synthesized bimetallic and trimetallic nanoparticles. The layers of EETMS and PVP adsorbed on the surface of discrete Pd nanoparticles with functional moieties: epoxy and other residual groups. The cross linking between these groups formed the cavities, which anchored the development of subsequent layers of nanoparticles in a gradual manner. Therefore the developed synthetic strategy (Liu et al, 2012) led to the formation of colloidal solutions (Zhang et al, 2011; Huggins et al, 2014; Venkatesan and Santhanalakshmi, 2010; Guo et al, 2010) which are highly stable and corresponding particles have low surface energies. These inferences are validated by comparing the stability of nanoparticles obtained via EETMS based template approach, with those synthesized using

conventional route (reduction using $NaBH_4$). Time dependent comparison (Figure 6.13) shows, the EETMS based nanoparticles stay monodispersed for longer duration than those obtained using the traditional pathway.

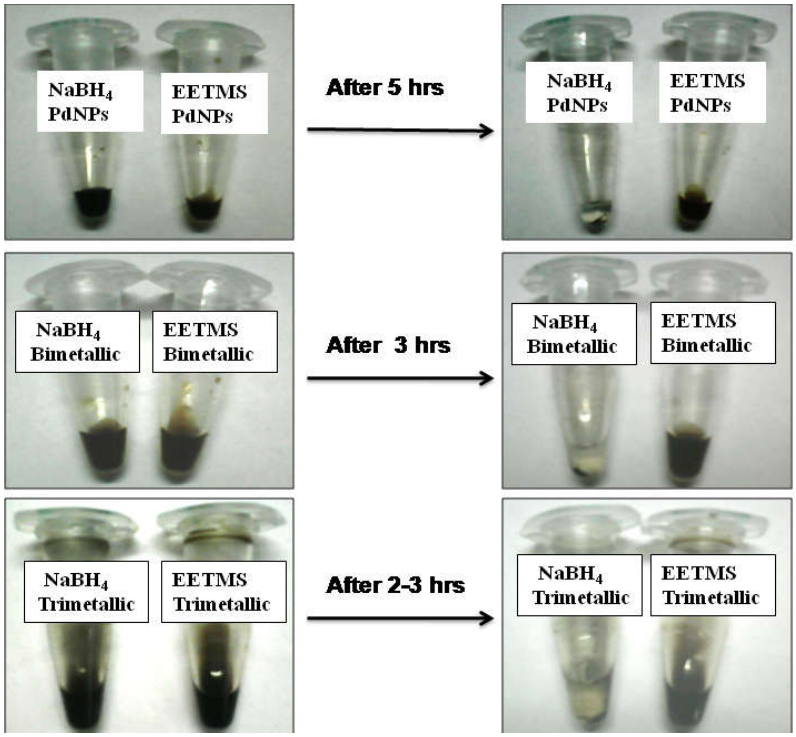

Figure 6.13. Comparison of conventional and present synthetic routes in terms of stability and templating properties.

6.4.2. Characterization of nanomaterials

The results of UV-Vis spectroscopy (Figure 6.1) clearly reveal that the identity of individual nanoparticle is retained, confirming that synthesized multimetallics (Ru@PdNPs and Ag@Ru@PdNPs) were nanocomposites rather than alloys. The formation of yellowish black colored colloidal solution of Ag@Ru@PdNPs and appearance of UV-Vis peak at ~ 420 nm (Figure 6.1), which is the characteristic peak of silver nanoparticles also confirm the formation of

trimetallic nanoparticles instead of the homogeneous mixture of individual nanoparticles. The TEM micrographs in Figures 6.2-6.4 show a remarkable reduction in size of palladium nanoparticles on the deposition of Ru and Ag. SAED patterns show polycrystalline nature of the synthesized multimetallic nanoparticles. Lattice planes corresponding to the successive metal (Pd Ru, Ag) nanoparticles are present in diffractograms of BNPs and TNPs. On the basis of above results, it was further resolved that the fabrication of triple-layered nanostructure, Ag@Ru@PdNPs was achieved, using the presynthesized Pd nanoparticles. XPS data provided a detailed insight regarding the changes in chemical states of the surface atoms in the prepared nanoscaled colloids. XPS spectra of Pd in BNPs and TNPs (Figure 6.8), show variations in intensity ratio and peak width, this is probably due to the presence of other metal atoms in the chemical envoirment. The Ru 3d spectra of multimetallic nanoparticles, shows the disappearance of usual doublet (Figure 6.9) splitted into peaks $3d_{5/2}$ and $3d_{3/2}$. Instead peak broadening is observed, which is due to flexible intrinsic and extrinsic factors, of which intrinsic broadening evolves due to inhomogeneity of material. Variations in chemical environment, widening of energy distribution among the orbitals in question, different elemental compositions and even sample conditions, are various other reasons, which contribute to the changes in characteristic spectra. Further, the shifting of peaks to higher binding energies in case of Ag 3d spectra of Ag@Ru@PdNPs is due to the electron transfer between the constituent metals.

6.4.3. Electrochemical analysis

In the present study we investigated the redox electrochemistry on four differently modified electrode systems. Based on the cyclic voltammetry results (Figure 6.11), the behavior of nanoparticle doped sol-gel thin film modified electrodes follow the order: ormosil-

Ag@Ru@PdNPs>ormosil-$[Fe(CN)_6]^{3-/4-}$-Ru@PdNPs>ormosil-$[Fe(CN)_6]^{3-/4-}$-PdNPs>ormosil-$[Fe(CN)_6]^{3-/4-}$.The increase in both anodic and cathodic peak current densities also follow the same order. The oxidation and reduction voltages are shifted to lower potential (below 0.3 V) along with decrease in the peak separation, observed in case of system **IV**. In order to predict the redox behavior of potassium ferricyanide in a more refined manner, both cathodic and anodic current densities are plotted against the different scan rates and as well as square root of scan (Figures 6.14). The results displayed in Figures 6.14, show the electron transfer properties of $[Fe(CN)_6]^{3-/4-}$ when incorporated in the nanostructured framework of sol-gel thin films. The peak current densities increased linearly upto 200 mVs^{-1} and became non-linear over higher scan rates.

6.4.4. Electrocatalytic behavior of modified electrodes

The catalytic performance of chemically modified electrode systems (**I-IV**) was evaluated from the investigations based on the voltammograms shown in Figure 6.12, in the presence (2) and absence (1) of L-ascorbic acid (Wu et al., 2012; Wang et al., 2013; Milakin et al., 2013). The fastest catalytic oxidation of ascorbic acid was observed on system IV (with TNPs) (Figure 6.12) as compared to other modified electrodes systems (I-III). It was better resolved, that system IV had excellent catalytic properties attributed to the ultrafine electronic distribution and involvement of active metal shells in probable core–shell framework of multimetallic nanoparticles, along with the significant behavior of redox mediator $[Fe(CN)_6]^{3-/4-}$.

Complementing the above investigation, catalytic aptitude of functionally modified electrode systems (I-IV), was further illustrated, by another electroanalytical technique called chronoamperometry. It involves a quantitative evaluation of catalytic behavior in terms of

catalytic rate constants (k_{cat}), where a system with highest magnitude of k_{cat}, is considered relatively more catalytic.

Table 6.3. Chronoamperometric characteristics of different chemically modified electrodes.

S.No.	Electrode Systems	k_{cat} ($M^{-1}s^{-1}$)
1.	Ormosil + $Fe(CN)_6^{3-/4-}$	0.3855
2.	Ormosil + $Fe(CN)_6^{3-/4-}$ + PdNPs	5.108
3.	Ormosil + $Fe(CN)_6^{3-/4-}$ + Ru@PdNPs	19.07
4.	Ormosil + $Fe(CN)_6^{3-/4-}$ + Ag@Ru@PdNPs	77.665

Figure 6.15 shows the chronoamperograms of modified electrodes, in (1) absence and (2) presence of AA (10 mM, 30 μL) setting a step potential of 0.3 V versus Ag/AgCl, for analysing I_{Ana} (current in presence of analyte) and I_L (current in absence of analyte). The quantity I_{Ana} /I was plotted against $t_{1/2}$ (square root of time in secs) as shown in insets to Figure 6.15. Over certain course of time (0–10 sec), the I_{Ana}/I found linearly dependent on $t_{1/2}$. The slope of this linear relation calculated as k_{cat}, for different systems (I-IV) are summarized in Table 6.3. Thus, the obtained values justify the enhanced catalysis on encapsulation of functional nanocatalysts

into sol–gel matrix, also proved the functional trimetallic nanoparticles to be the most potential catalyst, over the other reported catalysts.

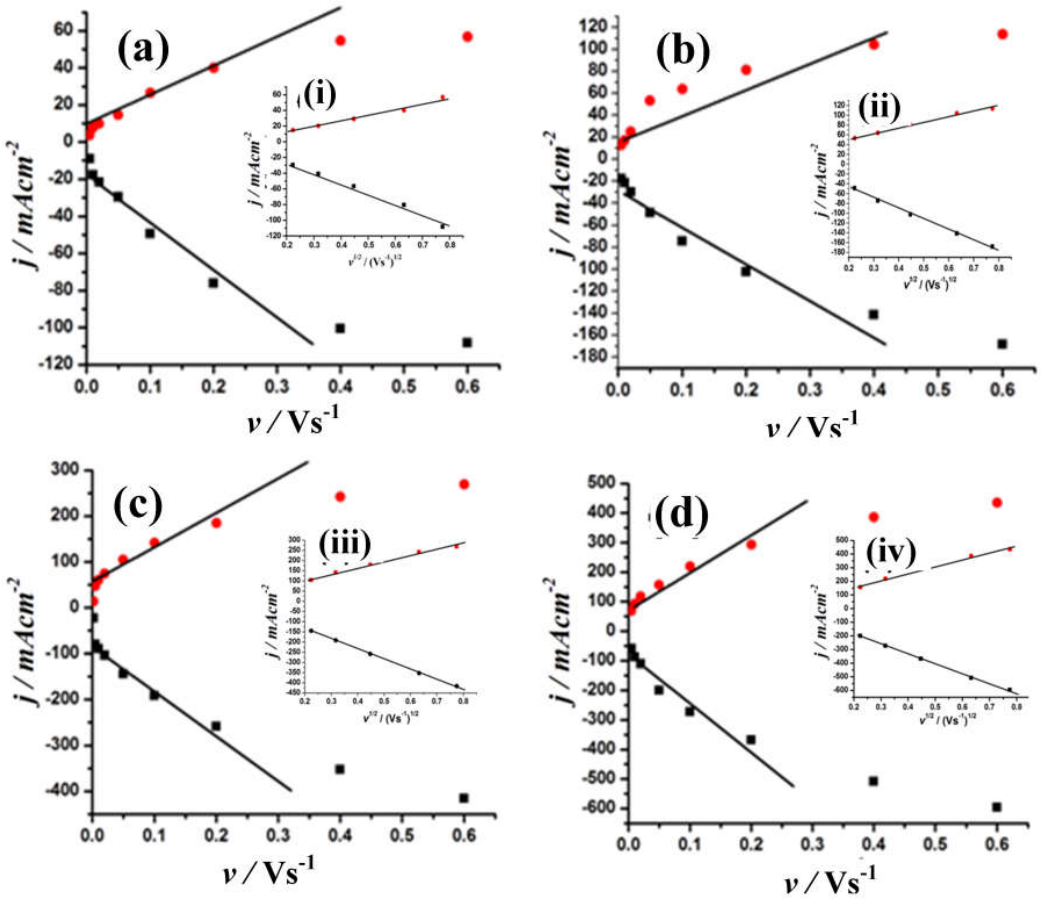

Figure 6.14. Plots of anodic and cathodic peak current densities against the scan rates for (a) Ormosil, (b) Ormosil-PdNPs, (c) Ormosil-Ru@PdNPs and (d) Ormosil-Ag@Ru@PdNPs. Inset pictures show the plots of anodic and cathodic peak current densities vs the square root of scan rates for (a) Ormosil, (b) Ormosil-PdNPs, (c) Ormosil-Ru@PdNPs and (d) Ormosil-Ag@Ru@PdNPs.

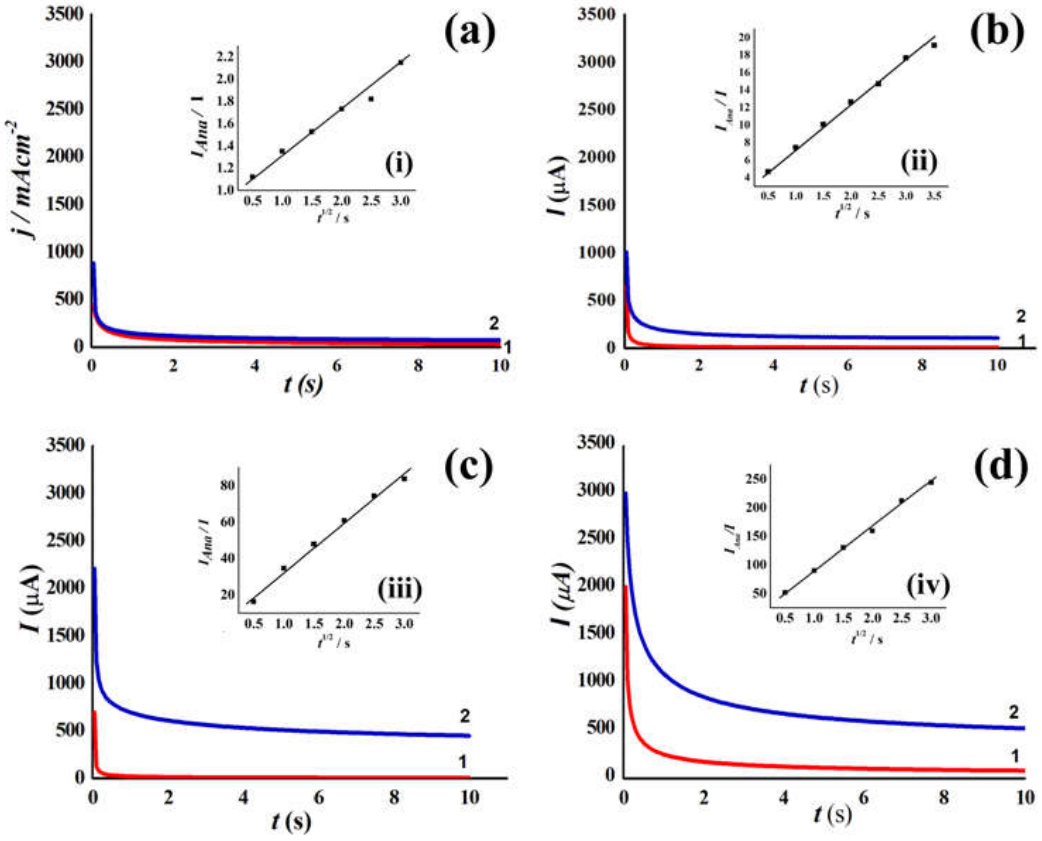

Figure 6.15. Chronoamperograms of $Fe(CN)_6^{3-/4-}$ encapsulated (a) Ormosil, (b) Ormosil-PdNPs, (c) Ormosil-Ru@PdNPs and (d) Ormosil-Ag@Ru@PdNPs in absence (1), and presence (2) of AA (1 mM, 30 L) in phosphate buffer (0.1 M, pH 7.0) at a scan rate of 10 mV/s. Inset: I_{Ana}/I versus $t_{1/2}$ plots.

6.5. CONCLUSION

Schematic route for functional alkoxysilane mediated synthesis of multimetallic counterparts of PdNPs has been demonstrated here. Presynthesized palladium nanoparticles produced by using EETMS, work as template to sequentially generate the subsequent double and triple layered nanoparticles, Ru@PdNPs(BNPs) and Ag@Ru@PdNPs(TNPs) respectively. The formation of

such nanostructures is confirmed by various characterization techniques. The functional ability of as-made nanomaterials enables its use in heterogeneous catalysis. These are easily assembled as nanoscaled thin film of organically modified silicate (ormosil), having potential for encapsulating the small molecules like potassium ferricyanide. The ormosil-encapsulated with redox couple $[Fe(CN)_6]^{3-/4-}$ display gradual improvement in redox electrochemistry as a function of monometallic, bimetallic and trimetallic nanoparticles. Chemically modified electrode systems were used as electrochemical sensors for the electrocatalytic oxidation of ascorbic acid. The TNPs doped sol-gel film (system IV), reflected the significant improvement in anodic current density relatively. Thus it is worth suggesting that nanoparticles fabricated in the present study bear enormous potential to discover their utility in future applications.